HHS Public Access

Author manuscript

Proc SPIE Int Soc Opt Eng. Author manuscript; available in PMC 2017 June 12.

Published in final edited form as:

Proc SPIE Int Soc Opt Eng. 2017 February 11; 10132: . doi:10.1117/12.2253745.

A CMOS-based high resolution fluoroscope (HRF) detector prototype with 49.5 μm pixels for use in endovascular image guided interventions (EIGI)

M. Russ[a], **A. Shankar**[a], **S. V. Setlur Nagesh**[a], **C. N. Ionita**[a], **D. R. Bednarek**[a], and **S. Rudin**[a]

[a]Toshiba Stroke and Vascular Research Center, University at Buffalo, Buffalo, NY

Abstract

X-ray detectors to meet the high-resolution requirements for endovascular image-guided interventions (EIGIs) are being developed and evaluated. A new 49.5-micron pixel prototype detector is being investigated and compared to the current suite of high-resolution fluoroscopic (HRF) detectors. This detector featuring a 300-micron thick CsI(Tl) scintillator, and low electronic noise CMOS readout is designated the HRF-$CMOS_{50}$. To compare the abilities of this detector with other existing high resolution detectors, a standard performance metric analysis was applied, including the determination of the modulation transfer function (MTF), noise power spectra (NPS), noise equivalent quanta (NEQ), and detective quantum efficiency (DQE) for a range of energies and exposure levels. The advantage of the smaller pixel size and reduced blurring due to the thin phosphor was exemplified when the MTF of the HRF-$CMOS_{50}$ was compared to the other high resolution detectors, which utilize larger pixels, other optical designs or thicker scintillators. However, the thinner scintillator has the disadvantage of a lower quantum detective efficiency (QDE) for higher diagnostic x-ray energies. The performance of the detector as part of an imaging chain was examined by employing the generalized metrics GMTF, GNEQ, and GDQE, taking standard focal spot size and clinical imaging parameters into consideration. As expected, the disparaging effects of focal spot unsharpness, exacerbated by increasing magnification, degraded the higher-frequency performance of the HRF-$CMOS_{50}$, while increasing scatter fraction diminished low-frequency performance. Nevertheless, the HRF-$CMOS_{50}$ brings improved resolution capabilities for EIGIs, but would require increased sensitivity and dynamic range for future clinical application.

Keywords

High-Resolution Fluoroscope (HRF); CMOS; Generalized Metrics; MTF; GMTF; DQE; GDQE

2. INTRODUCTION

In order to provide the greatest utility to interventionists during neuro-endovascular x-ray image guided interventions (neuro-EIGIs), new and novel detectors are continually evaluated on the basis of their inherent abilities, and their performance as part of an imaging chain. A

Correspondence to: M. Russ.

new detector prototype has been introduced to this suite of detectors designed to provide high resolution during neuro-EIGIs. This new detector, designated the HRF-$CMOS_{50}$ (Mammo7 prototype, Teledyne-DALSA, Waterloo, Canada) to describe its less than 50 micron pixel pitch and low electronic noise CMOS readout, is an indirect CsI(Tl)-based detector that features a 300 micron thick scintillator.

The performance of this detector was characterized using existing standard metrics including instrumentation noise equivalent exposure (INEE)[1] and sensitivity tests, the modulation transfer function (MTF), noise power spectra (NPS), noise equivalent quanta (NEQ), and the detective quantum efficiency (DQE) metrics, and compared to existing high resolution detectors' abilities. These existing detectors have been previously characterized through comprehensive metrics analysis, and include the MAF-CCD[2] (35 micron pixel pitch, 500 micron CsI thickness), the HRF-$CMOS_{75}$ (Dexela 1207, Perkin-Elmer, Waltham, MA, 75 micron pixel pitch, 600 micron CsI thickness)[3], and a standard flat panel detector (FPD) (Paxscan 2020, Varian Medical Systems, Palo Alto, CA, 194 micron pixel pitch, 600 micron CsI thickness).

The detector experiences performance degradation when other aspects of an imaging chain are considered. This impact was quantified using the generalized performance metrics, which are designed to include the effects of a finite focal spot size exacerbated by magnification greater than unity, and scatter blur in addition to the inherent performance of a given detector.

3. MATERIALS AND METHODS

The first tests of the HRF-$CMOS_{50}$ detector included sensitivity, linearity, and instrumentation noise equivalent exposure (INEE)[1] measurements. The detector INEE was determined by acquiring 100 images over a wide range of exposures, starting from the lowest fluoroscopy exposure level the x-ray source could output for a 70 kVp spectrum, up to the highest possible output using digital angiography. The fluoroscopic and angiographic results were plotted separately, as differences in sensitivity are expected due to differing pulse shaping and x-ray filtration for the exposure modes. These images were gain and offset corrected, and the variance of the images was calculated using ImageJ. The variance for a set of images was plotted against the exposure, measured in mR/frame, and a linear regression curve was fitted to the data. The y-intercept was allowed to vary. The INEE was calculated from the quotient of the y-intercept and the slope of this fit. The linearity of the detector was determined from a plot of the same data, separated by exposure type. From the previously acquired images, the mean of each set of images was calculated using ImageJ and both the fluoroscopy and digital angiography data were plotted separately versus exposure in mR/frame. A linear fit was applied to both data sets with the y-intercept constrained to 0. The slope from this fit gave the sensitivity of the detector in DN/(mR/frame) and the linearity of the detector for each exposure type was given by the correlation coefficient of the fit.

To describe the resolution abilities of this new detector, the presampled MTF was calculated in accordance with the edge method published by Samei et al[4]. A sheet of lead was sandwiched between two sheets of aluminum, and precisely machined into a straight edge.

This edge was suspended against the detector face at an angle between 1°–3°. The SID was set to be 115 cm to minimize scatter. A set of 100 images were acquired of the edge for each x-ray energy between 60 and 100 kVp, in directions parallel and perpendicular to the direction of pixel readout. These images were gain and offset corrected, then averaged together to minimize quantum noise before use in the MTF calculation. The edge spread method requires a priori knowledge of the edge angle, which was found using the Hough transform, before reprojecting along the edge to create an oversampled edge spread function (ESF), which is differentiated to obtain a line spread function (LSF). The Fourier transform of the LSF is then taken, resulting in the presampled MTF.

The detector MTF was also calculated using the Noise Response (NR) method. This new method, proposed by Kuhls-Gilchrist et al[5], is more robust in that it does not utilize an edge, line or pinhole, but instead relies on the exposure-dependent quantum noise component of the noise power spectrum acquired from flat images to calculate the MTF. When applied to the standard processes of indirect detectors, cascaded linear systems theory gives the definition of detector noise response to be defined as

$$NPS(u,v)=\Delta x\Delta y\left[g_{tot}\frac{T_{sys}^2(u,v)}{A_s(u,v)}+\frac{g_{dig}}{F_p}\right]\Phi_{dig}+NPS_{add}(u,v), \quad (1)$$

where Δx and Δy represent pixel pitch, g_{tot} is the total gain of the detector, T_{sys} is detector MTF, A_s is the frequency dependent Swank factor, g_{dig} is the digitization gain, F_p is the pixel fill factor, Φ_{dig} represents the average digital detector value for a given fluence, and NPS_{add} is the additive noise component. For gain and offset corrected images obtained using a linear detector, this equation can be simplified to

$$Slopes(u,v)=\frac{\Delta x\Delta y g_{tot}}{A_s(u,v)}T_{sys}^2(u,v)+\frac{\Delta x\Delta y g_{dig}}{F_p}, \quad (2)$$

where Slopes refers to the slope of a linear fit of the NPS calculated from sets of 50 or more images acquired at at least six exposures, plotted versus mean signal for a set of images. If the slopes are known, the detector MTF can be solved for, either directly if all variables are known, or by fitting Equation 2 using either a Gaussian mixture function or an error function.

The normalized noise power spectrum is defined as the square of the modulus of the Fourier transform of the variations of the average pixel value in a flat image, normalized to the square of the average signal value, and describes the frequency- and exposure-dependent noise response of the detector. Images were acquired for use in NNPS calculations, using an SID of 115 cm at five different energies between 60 kVp–100 kVp, at three exposure levels: 0.3 mR/frame, 0.5 mR/frame, and 0.7 mR/frame. A NNPS was also calculated for the 70 kVp beam at an exposure of 0.04 mR/frame for comparison with other high resolution detector metrics. These exposure levels were dictated by the output limitations of the x-ray

tube for all five energies. All images were gain and offset corrected before the NNPS calculation was performed. The AAPM NPS task group recommends a minimum of 64 overlapping sub-regions for a 256 × 256 sub-region size[6], and for these calculations that criteria was exceeded. The 2D NNPS was calculated from 60 frames, then radially averaged.

The noise equivalent quanta (NEQ) was calculated for all five energies at each of three exposure levels from the square of the MTF divided by the NNPS from zero frequency to the detector Nyquist frequency of 10 cycles/mm. The detective quantum efficiency (DQE) was calculated from the NEQ divided by the number of quanta per mm^2, which was calculated separately for each energy and exposure combination.

Our group has developed a set of generalized metrics[7] which enhance the existing standard suite of metrics and describe the performance of the detector as part of an imaging system. The generalized MTF (GMTF) defined at the detector plane, which is shown below in Equation 3, includes the effects of finite focal spot size exacerbated by magnification, and a non-zero scatter fraction.

$$GMTF(u,\rho,m)=[(1-\rho)MTF_f((m-1)u)+\rho MTF_s(u)]MTF_d(u) \quad (3)$$

Here, u is the spatial frequency in the detector plane, ρ is the scatter fraction, m is the object magnification, and MTF_d is the presampled detector MTF. The MTF_f represents the focal spot MTF in the anode plane, which is defined as the modulus of the Fourier transform of the focal spot point spread function. The scatter blur MTF, or MTF_s, is defined as the modulus of the Fourier transform of the differentiated scatter edge spread function and is defined in the detector plane.

The generalized NEQ (GNEQ) can be calculated from the GMTF and the generalized NNPS (GNNPS), which can simply be calculated from the detector NNPS scaled to the object plane by the square of the magnification, as shown in Equation 4, where X represents exposure.

$$GNNPS(u,X,\rho,m)=\frac{NNPS_d(\frac{u}{m},X,\rho)}{m^2} \quad (4)$$

The GNNPS calculated at the detector plane is simply the NNPS; magnification would be equal to unity, and no scaling would occur. The GNEQ definition in the object plane naturally follows as defined in Equation 5.

$$GNEQ(u,X,\rho,m)=\frac{GMTF^2(u,\rho,m)}{GNNPS(x,X,\rho,m)} \quad (5)$$

The generalized DQE in the object plane is defined in Equation 6. Here, Φ_{in} is the number of x-ray quanta per mm^2 reaching the detector face, and takes into consideration the relative intensity of each x-ray photon energy in a bremsstrahlung spectrum for all five energies at each exposure level.

$$GDQE(u,X,\rho,m)=\frac{GNEQ(u,X,\rho,m)}{\Phi_{in}(X,m)} \quad (6)$$

4. RESULTS

4.1 Standard Metrics

The result of the INEE measurement is shown below in Figure 1. After fitting the plotted data with a linear regression curve, the quotient of the intercept and the slope was determined to be 7.36 μR. This INEE is relatively high compared to those of the HRF-$CMOS_{75}$ in both its high and low sensitivity modes, and the MAF-CCD, which are 0.55 μR,[2] 2.77 μR,[2] and 0.22,μR [1] respectively.

The results of the sensitivity and linearity measurements are shown in Figure 2. Both the fluoroscopy and digital angiography images showed strong linearity, and the sensitivities were determined to be 1.96 DN/μR and 1.91 DN/μR, respectively. Similar to the INEE results, this sensitivity is low when compared to the other high resolution detectors, whose sensitivities are 31.55 DN/μR and 9.87 DN/μR for the high and low sensitivity modes of the HRF-$CMOS_{75}$ [2].

The results of the MTF experiment are shown in the left plot in Figure 3. As expected, the MTF varies little with x-ray energy. The MTFs calculated using the standard edge method are plotted in a solid line, and the MTFs determined using the noise response (NR) method are plotted in a dotted line. Both estimates of the detector's spatial resolution response show agreement from 0 to 4 cycles/mm. The NR method estimates a lower MTF than the edge method from 4 to 9 cycles/mm, with a percent devation of 17% at 6 cycles/mm. The 70 kVp MTF was selected for comparison with the existing high resolution detectors' MTFs and is shown in the right plot in Figure 3. The improved resolution performance of the new detector compared to existing detectors is dramatic. The heightened resolution of the HRF-$CMOS_{50}$ is due partially to the reduced pixel size and the reduction in blurring in the 300 micron thick CsI(Tl) scintillator as compared to those phosphors used in the other detectors, which range in thickness from 500–600 microns.

The normalized noise power spectra for energies 60 kVp, 70kVp, 80 kVp, 90kVp, and 100 kVp are plotted for the three exposure levels in Figure 4 (right). For all three exposures, the NNPS for the higher energies were calculated to be higher than that of the 60 and 70 kVp spectra. Upon closer inspection of the flat images used for this calculation it was determined that the CMOS camera was incurring direct x-ray hits due to the thin scintillator, and inevitably, the prevalence of direct hits increased with higher x-ray photon energies. This increase is shown in Figure 4 (left). To mitigate this, the flat images acquired for all beam

energies were manually thresholded to eliminate the direct hits from the image, and the detector NNPS were recalculated. Future detectors of this design could include not only a thicker phosphor but also a fiber-optic plate to shield against direct exposure to the CMOS with the risk of some loss in resolution.

From the MTF and thresholded NNPS results, the NEQs for all three energies and exposure levels were calculated, and are displayed in Figure 5 (left). The NEQs show no dependence on x-ray energy, and the separation by exposure is expected. Additionally, the NEQ was calculated for a 70 kVp x-ray beam at an exposure of 0.04 mR/fr to be compared with results from the other detectors.

Calculation of the DQE required an estimate of the x-ray fluence for normalization of the NEQ. The x-ray spectra for each energy were simulated using SpekCalc[8], based on known x-ray beam kVp and measured half value layers. The results of these simulations are shown in Figure 6. The DQE results are shown in Figure 5 (right). The DQEs calculated for each beam energy showed no dependence on exposure, as expected due to normalization. However, as x-ray beam energy increased the DQE(0) value exhibited a decrease from 0.48 for 60 kVp down to 0.38 for 100 kVp. The HRF-$CMOS_{50}$ detector has a 300 micron phosphor, and for increasing x-ray energies the number of photons absorbed in the phosphor, or the quantum detective efficiency (QDE), should decrease.

The NEQ and DQE calculated for the HRF-$CMOS_{50}$ for a 70 kVp beam at exposure 0.04 mR/frame are shown in Figure 7, plotted against the comparable measurements for the MAF-CCD, HRF-$CMOS_{75}$, and the FPD detector. These results highlight the differences in sensitivity between the HRF-$CMOS_{50}$ and the other high resolution detectors due to a thinner phosphor and a less sensitive CMOS camera. The HRF-$CMOS_{50}$ exhibits similar NEQ and DQE values to the MAF-CCD between 2 and 6 cycles/mm, but does not reach the ability of the comparable detector, the HRF-$CMOS_{75}$ for this exposure.

4.2 Generalized Metrics Analysis

The measured results from the MTF, NNPS, NEQ, and DQE were used in generalized metric performance analysis of the HRF-$CMOS_{50}$ detector. The MTF_f was calculated from pinhole images of two different focal spot sizes; small (SFS, 0.3mm) and medium (MFS, 0.6mm) for use in the calculation of the GMTF. Shown in Figure 8 (left) are the results of the GMTF calculations for both focal spot sizes at two magnifications (M = 1.05, 1.2) for the 70 kVp MTF. The GMTFs calculated for low magnification show little degradation, particularly when the SFS is considered. The blurring due to the finite size of the focal spot is clearly exacerbated when the higher magnification case is considered, as evidenced by the decrease in GMTF value at the higher spatial frequencies.

The GMTF results calculated using a small focal spot and low magnification with increasing scatter fractions are shown in Figure 8 (right). The scatter fractions selected, 0.1, 0.3, and 0.5, correspond to the scatter fraction reaching the detector face for radiation field sizes 5 cm^2, 20 cm^2, and 60 cm^2, with a human head equivalent phantom placed 2.5 cm from the detector[7]. With increasing scatter fraction, the apparent degradation at the lowest spatial frequencies is immense.

The GDQEs were calculated for all aforementioned focal spot sizes, magnifications, scatter fractions, and are plotted in Figure 9. As evidenced with the GMTF results, the GDQE is further degraded at the high spatial frequencies with increasing focal spot size and magnification (as shown in Figure 9 (left)). The GDQEs also suffer heavy degradation at the low spatial frequencies due to increased scatter fraction. This result is shown in Figure 9 (right).

Shown in Figure 10 are images acquired of an anthropomorphic head phantom with a pipeline stent placed on the front. Using fluoroscopic exposure levels, the noise in the image severely degrades the image quality, making the comparable images from the HRF-$CMOS_{75}$ the more desirable and more useful image. However, when a digital angiography exposure is used, the quantum noise is significantly reduced for the HRF-$CMOS_{50}$ and the unique resolution capabilities are visible. The detail of the stent struts provided surpasses that given by the HRF-$CMOS_{75}$.

DISCUSSION

Though not used in the subsequent metrics analysis, the MTFs calculated using the noise response method showed agreement with the MTFs calculated using the edge method. The HRF-$CMOS_{50}$ NEQs and DQEs were calculated from the noise response MTFs, and yielded similar results to the edge method MTFs, as expected. These NEQ and DQE results are shown in Figure 11. Future analysis will be performed to examine the differences between the edge method and the noise response method MTFs.

CONCLUSIONS

The HRF-$CMOS_{50}$ presents an impressive opportunity for improved resolution capabilities for EIGIs, as evidenced by the MTF and GMTF results shown in this work. The HRF-$CMOS_{50}$ exhibited an MTF value of 0.2 at 6 cycles/mm, which is double that of the HRF-$CMOS_{75}$ at the same frequency, and showed even greater improvement over the existing detectors for mid-range frequencies (3–5 cycles/mm). However, this detector, originally designed for mammography, would require greater electronic gain dynamic range and a thicker CsI phosphor to put the sensitivity in the desired range for neuro-endovascular x-ray image guided procedures. It is clear from the comparisons of the standard metrics with the existing high resolution detectors that the HRF-$CMOS_{50}$ currently lacks the sensitivity to be a competitive detector at interventional exposure levels. If the HRF-$CMOS_{50}$ could achieve sensitivity similar to that of the existing suite of detectors, this detector could bring as of yet unseen resolution capabilities to the interventional suite.

Acknowledgments

Partial support from NIH grant R01-EB002873, cooperation from Teledyne Dalsa Inc., and an equipment grant from Toshiba Medical Systems Corp.

References

1. Yadava GK, Kuhls-Gilchrist AT, Rudin S, Patel VK, Hoffman KR, Bednarek DR. A practical exposure-equivalent metric for instrumentation noise in x-ray imaging systems. Phys Med Biol. 2008; 53:0039–9155.
2. Jain, A. Design, construction, and evaluation of new high resolution medical imaging detector/ systems. State University of New York at Buffalo, ProQuest, UMI Dissertations Publishing; 2010. p. 3723477
3. Jain A, Bednarek DR, Rudin S. Experimental and theoretical performance analysis for a CMOS-based high resolution image detector. Proc SPIE Int Soc Opt Eng. 2014 Mar 19.9033:9033P.
4. Samei, Flynn, Reimann. Measuring the presampled MTF of digital radiographic systems. Medical Physics. 1998; 25(1):102–113. [PubMed: 9472832]
5. Kuhls-Gilchrist A, Jain A, Bednarek DR, Hoffmann KR, Rudin S. Accurate MTF measurement in digital radiogrpahy using noise response. Med Phys. 2010; 37:0094–2405.
6. Maidment, et al. AAPM Report: Report of Diagnostic Imaging Task Group No. 16 Draft version 3.0. 2004. Standard for Measurement of Noise Power Spectra.
7. Kyprianou IS, Rudin S, Bednarek DR, Hoffman K. Generalizing the MTF and DQE to include x-ray scatter and focal spot unsharpness: application to a new microangiographic system. Med Phys. 2005; 32:613–26. [PubMed: 15789608]
8. http://spekcalc.weebly.com/

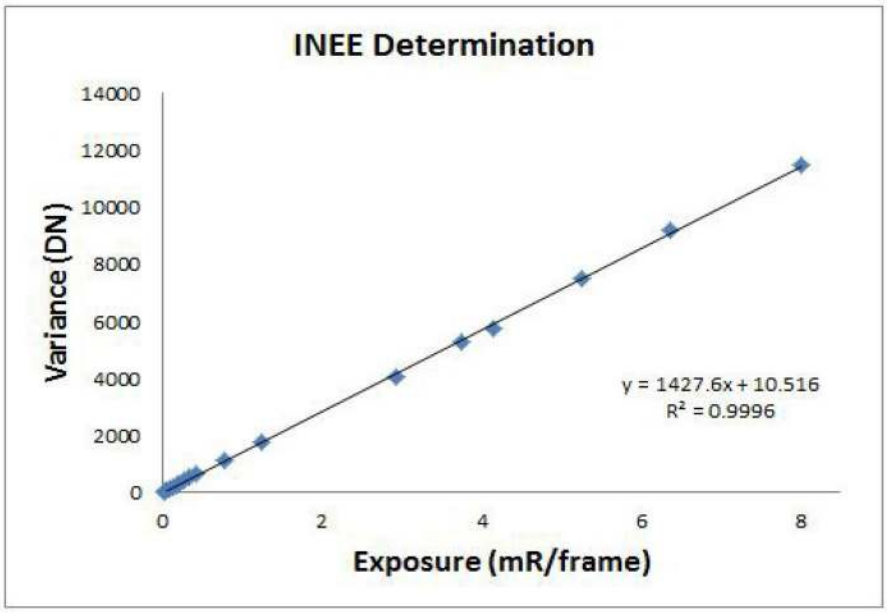

Figure 1.
A linear fit of the variance versus exposure allows for the calculation of the HRF-CMOS50 INEE.

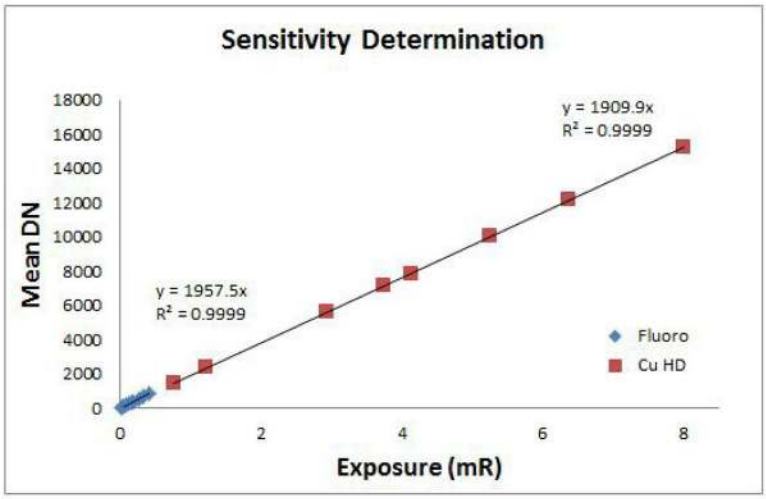

Figure 2.

The sensitivity data plotted for the HRF-CMOS50 detector using images acquired under fluoroscopic (plotted in blue) and digital angiographic (plotted in red) exposure levels.

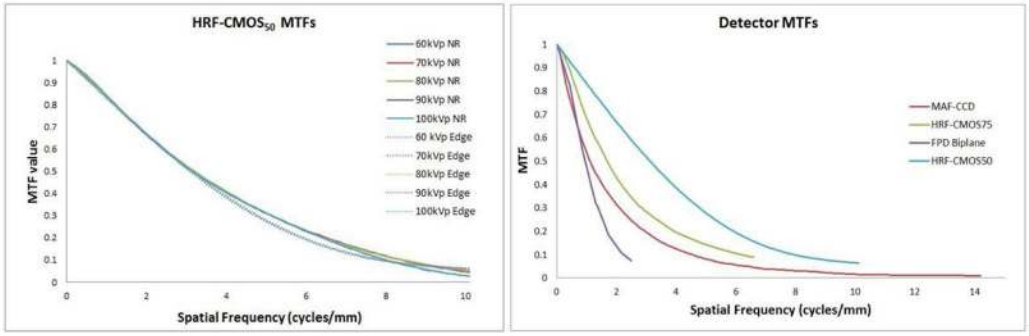

Figure 3.

(Left) The MTFs plotted for the HRF-CMOS detector, and (right) the MTF of the HRF-CMOS detector at 70 kVp plotted alongside the MTFs of the other HRF detectors.

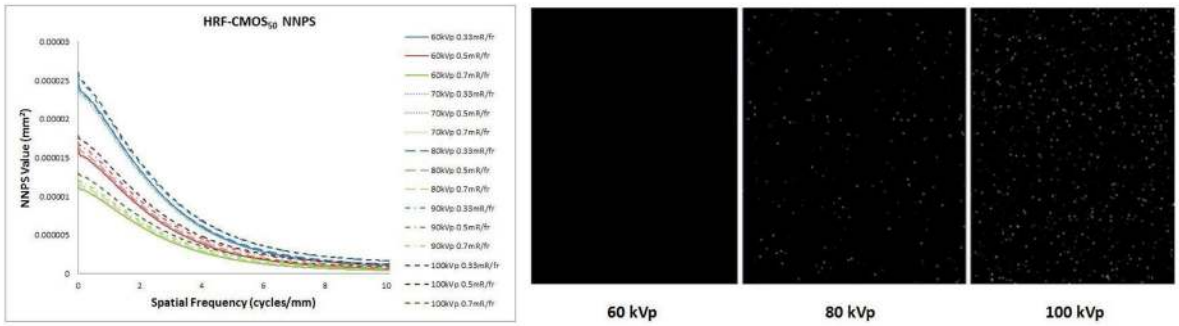

Figure 4.

(Left) The noise power spectra for all five beam energies and three different exposures (0.3, 0.5, and 0.7 mR/fr). (Right) Images showing the increasing number of direct hit events with increasing beam energy.

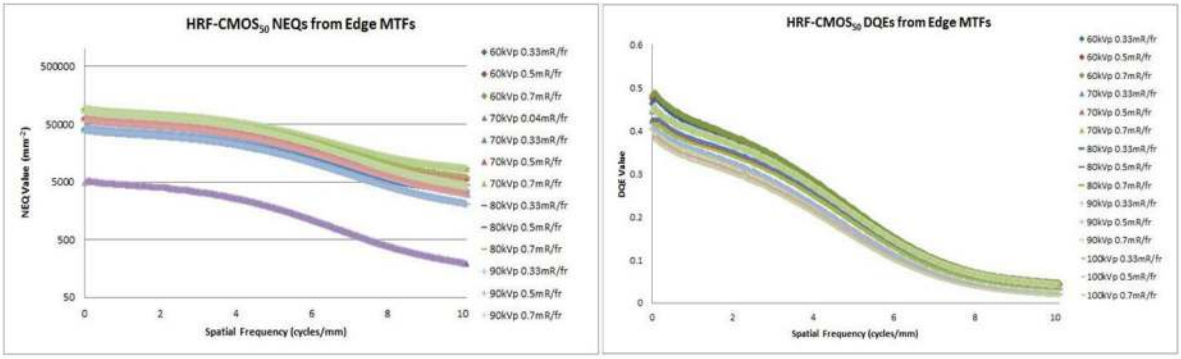

Figure 5.

(Left) The HRF-CMOS50 NEQs, calculated from the known MTF and NNPS for all five energies considered in this project. Also included is the NEQ at 70 kVp calculated at 0.04 mR/fr for comparison with the existing high resolution detector metrics. (Right) The HRF-CMOS50 DQEs calculated for all energies and exposures.

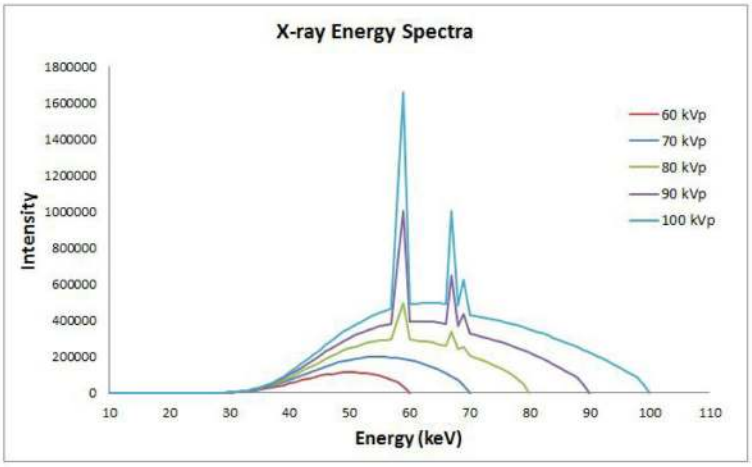

Figure 6.

The simulated spectra, calculated from the known x-ray kVp and half value layer for all five energies considered in this project.

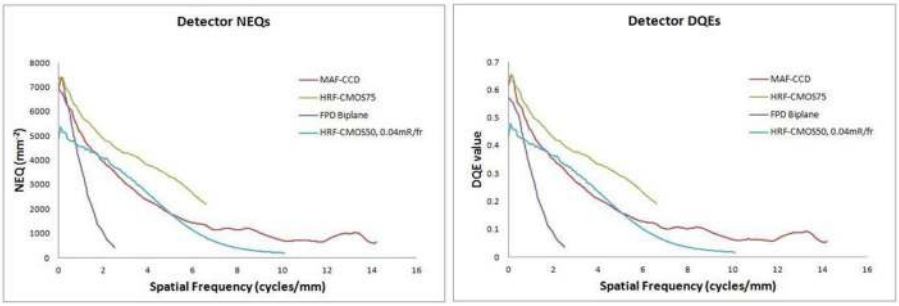

Figure 7.

The NEQ (left) and DQE (right) of the HRF-CMOS50 for a 70 kVp beam at exposure 0.04 mR/frame compared to the comparable measurements for the existing suite of detectors.

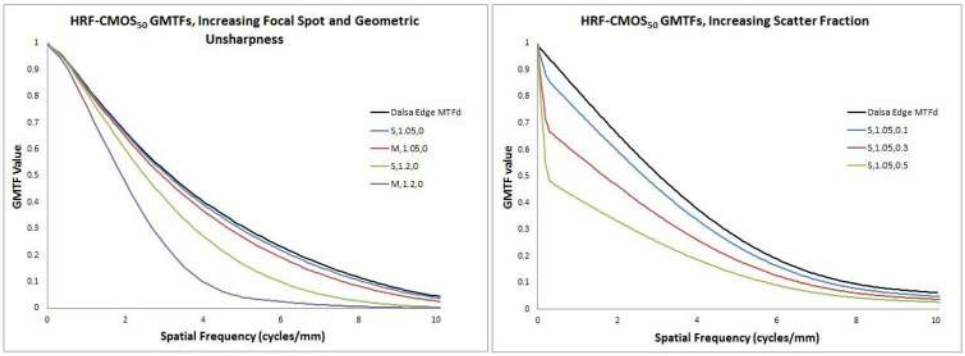

Figure 8.

Calculated GMTFs for the HRF-CMOS50. On the left plot, GMTFs concerning increasing focal spot size and increasing magnification. On the right, GMTFs calculated for low magnification with a small focal spot, showcasing the effects of increasing scatter fraction.

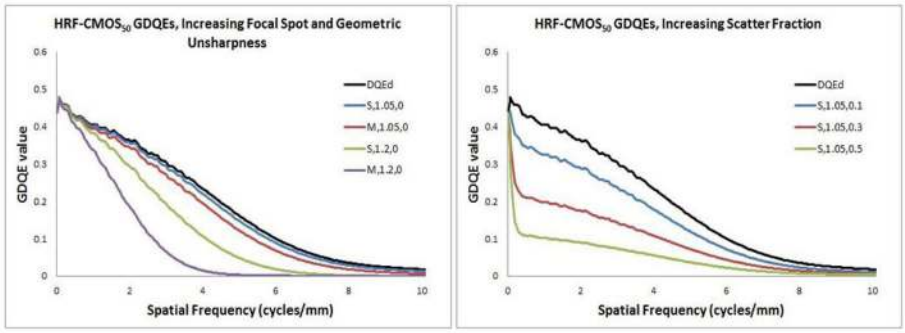

Figure 9.

Calculated GDQEs for the HRF-CMOS50. On the left plot, GDQEs concerning increasing focal spot size and increasing magnification. On the right, GDQEs calculated for low magnification with a small focal spot, showcasing the effects of increasing scatter fraction.

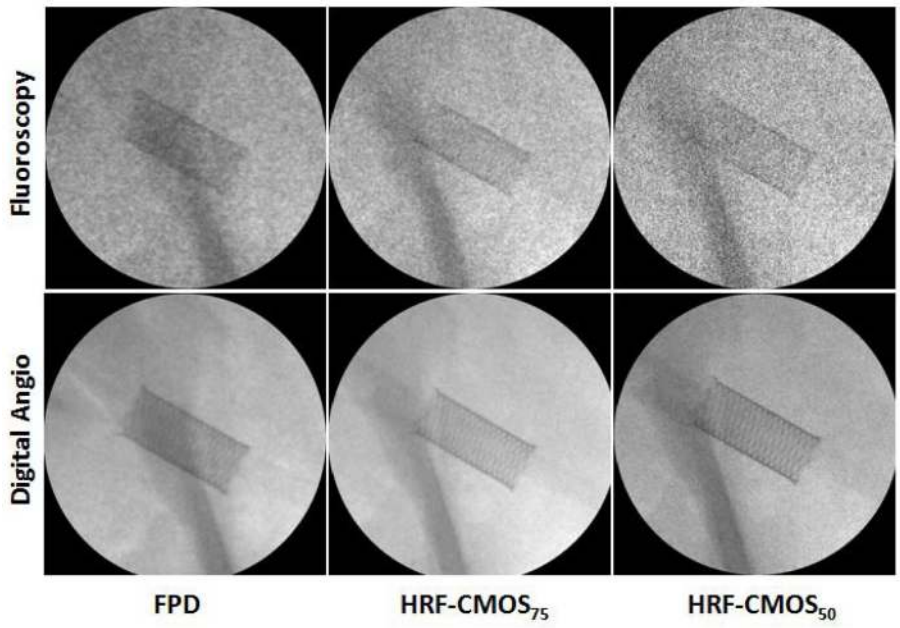

Figure 10.
Images acquired using the FPD, HRF-CMOS75, and HRF-CMOS50 for the same imaging task. The top row show fluoroscopic exposure levels, and the bottom row show digital angiographic exposure levels.

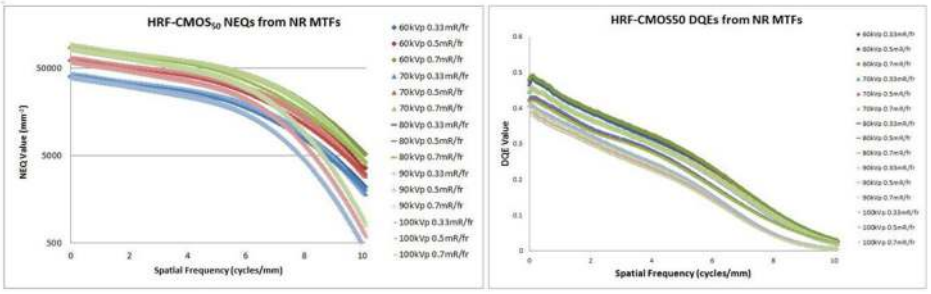

Figure 11.

The NEQs (left) and the DQEs (right) calculated with the MTFs determined via the noise response method.